Revision1

High-pressure experiments on phase transition boundaries between corundum, Rh_2O_3(II) and $CaIrO_3$-type structures in Al_2O_3

Jinya Kato,[1] Kei Hirose,[1,2,]* Haruka Ozawa,[1,2] and Yasuo Ohishi[3]

[1]Department of Earth and Planetary Sciences, Tokyo Institute of Technology, Meguro, Tokyo 152-8551, Japan

[2]Institute for Research on Earth Evolution, Japan Agency for Marine-Earth Science and Technology, Yokosuka, Kanagawa 237-0061, Japan

[3]Japan Synchrotron Radiation Research Institute, Sayo, Hyogo 679-5198, Japan

* E-mail: kei@geo.titech.ac.jp

ABSTRACT

Phase transitions in Al_2O_3 between corundum, Rh_2O_3(II)-type, and $CaIrO_3$-type (post-perovskite-type) phases were examined at high pressure and high temperature in a laser-heated diamond-anvil cell (DAC) based on in-situ x-ray diffraction measurements. The locations of corundum-Rh_2O_3(II) and Rh_2O_3(II)-$CaIrO_3$ boundaries were precisely determined

by conducting both forward and backward reactions experiments. The results demonstrate that corundum undergoes phase transition to Rh_2O_3(II)-type structure above 106 GPa at 1800 K with a negative Clapeyron slope of -6.5 ± 1.5 MPa/K, generally consistent with earlier experimental and theoretical works. The Rh_2O_3(II)-type phase further transforms into $CaIrO_3$-type above 170 GPa at 2300 K, indicating the transition pressure much higher than earlier experimental work but in agreement with reported GGA calculations. The Clapeyron slope of this phase transition was found to be high negative (-20 ± 5 MPa/K).

Keywords: phase transition, high pressure, Al_2O_3, corundum, Rh_2O_3, $CaIrO_3$, post-perovskite

INTRODUCTION

Aluminum oxide is an important ceramic material and widely used as a pressure standard in static DAC experiments (Cr^{3+}-bearing corundum, ruby). In addition, Al_2O_3 is one of the major components in the Earth's crust and mantle. It is an important impurity in silicate perovskite and post-perovskite, primary constituents in the lower mantle, and strongly affects their stabilities above the core-mantle boundary (e.g., Akber-Knutson et al. 2005; Tateno et al. 2005; Tsuchiya and Tsuchiya 2008). Also, Al_2O_3 corundum may occur as a discrete mineral in

subducted highly Al-enriched materials (Komabayashi et al. 2009; Kawai et al. 2009). The high-pressure (P) and high-temperature (T) behavior of Al_2O_3 is thus of great importance in both materials science and deep Earth science.

Al_2O_3 crystallizes as corundum at low pressures. Cohen (1987) first examined a phase transition from corundum to Rh_2O_3(II)-type structure by theory. Since then, a number of theoretical calculations have been made to predict the transition pressure using different models (Marton and Cohen 1994; Thomson et al. 1996; Duan et al. 1998; Caracas and Cohen 2005; Tsuchiya et al. 2005). Experiments performed by Jephcoat et al. (1988) showed that the corundum structure was preserved up to 175 GPa at ambient temperature. The first experimental confirmation of Rh_2O_3(II)-type phase was made by Funamori and Jeanloz (1997). They observed the phase transition approximately at 100 GPa and 1000 K. The most recent experimental work by Lin et al. (2004) reported the transition above 96 GPa but the phase boundary (temperature dependence) was not determined.

$CaIrO_3$-type Al_2O_3 was originally reported by the theoretical works performed by Oganov and Ono (2005), Caracas and Cohen (2005), and Tsuchiya et al. (2005). It is isostructural with $MgSiO_3$ post-perovskite phase (e.g., Hirose 2006). Oganov and Ono (2005) and subsequent experimental work by Ono et al. (2006) demonstrated the phase transition boundary between

52 Rh_2O_3(II)- and $CaIrO_3$-type structures at 130 GPa and 1000 K, approximately similar to that of
53 perovskite to post-perovskite phase transition in $MgSiO_3$. On the other hand, Caracas and
54 Cohen (2005) and Tsuchiya et al. (2005) predicted the transition pressure above 150 GPa at 0 K.
55 Additionally, the high negative Clapeyron slope of the boundary was reported by theory
56 (Tsuchiya et al. 2005), but it has not been verified by experiments yet.

57 Here we determined the phase transition boundaries in Al_2O_3 between corundum,
58 Rh_2O_3(II)-, and $CaIrO_3$-type structures, based on the in-situ x-ray diffraction (XRD)
59 measurements at the synchrotron radiation source. These phase transitions were found to be
60 rather sluggish. We therefore performed both forward and backward experiments using a mixed
61 sample containing low-pressure and high-pressure phases together, which enabled us to
62 precisely locate the pressure and Clapeyron slope of the equilibrium phase transition
63 boundaries.

64

65 **EXPERIMENTAL METHODS**

66 The high *P*-*T* conditions were generated in a laser-heated DAC. We used a fine powder of
67 Al_2O_3 as a starting material. A pelletized sample was coated with Pt, which served both as an
68 internal pressure standard and as a laser absorber. It was loaded into a 30 or 50-μm hole in a

rhenium gasket, together with a pressure medium of SiO_2 glass. Beveled diamond anvils with 90 or 150-μm culet were used for compression. The sample was heated from both sides using a fiber laser. Temperature was measured by the spectroradiometric method (Ohishi et al. 2008). Typical temperature profiles across the heating spot are provided in Fig. 1.

Angle-dispersive XRD spectra of the sample were collected at high pressure and temperature primarily on the CCD detector (Bruker APEX), which has 1024 × 1024 pixel dimensions with a pixel size of 60-μm × 60-μm, at the beamline BL10XU of SPring-8. Exposure time was 10 to 30 sec. A monochromatic incident x-ray beam with a wavelength of 0.4115 to 0.4144 Å was collimated to 15-μm in diameter. Two-dimensional XRD images were integrated as a function of 2-theta angle in order to give a conventional one-dimensional diffraction profile using the fit-2D program (Hammersley et al. 1996).

The variation in temperature within 15-μm area from which x-ray diffractions were collected was less ±10% (Fig. 1). Pressure was calculated from the unit-cell volume of platinum based on its *P*-*V*-*T* equation of state proposed by Holmes et al. (1989). The errors in pressure were less than ±3.7 GPa at high temperature, derived mainly from large uncertainty in temperature in the application of *P*-*V*-*T* equation of state. We repeated the heating cycles with increasing/decreasing the load pressure in a single run (Tables 1 and 2).

We determined the stable phase at each *P-T* condition, based on 1) the appearance of high-pressure phase, 2) grain growth observed in two-dimensional XRD image or XRD peak growth when the sample included a single phase, and 3) peak growth or reduction when two phases coexisted.

RESULTS

Boundary between corundum and Rh_2O_3(II)-type structures

We have performed one run (run #1) at relatively low pressure range for corundum-Rh_2O_3 boundary (Table 1). The sample was first compressed to 87 GPa at room temperature. The broad XRD peaks from corundum were observed before heating (Fig. 2a). Such corundum peaks became sharp and spotty when the sample was first heated to 2390 K for 8 min at 99 GPa (heating cycle #1 in Table 1), indicating the grain growth and thus the stability of corundum at such *P-T* condition. After quenching temperature, the sample was further compressed at 300 K and reheated to 2060 K at 121 GPa (cycle #2). The peaks of Rh_2O_3 (II)-type structure appeared in 38 min. Using such corundum + Rh_2O_3(II) coexisting sample, we further examined the phase stability based on the growth/reduction of the corresponding XRD peaks. For this purpose, only corundum 104 line and Rh_2O_3(II) 211 and 021 lines were used to avoid peak overlapping. Phase

stability was judged from the change in relative intensities (peak areas) given in Table 1. Subsequently the sample was decompressed and again heated to 2180 K at 105 GPa (cycle #3). We observed the growth of the Rh_2O_3(II) peaks in 8 min (Figs. 2b and 3b). When the temperature was decreased to 1870 K, the corundum peaks conversely grew relative to those of Rh_2O_3(II) (Figs. 2c and 3a), indicating the reversal phase transition at this *P-T* condition. Upon following heating both at 2560 and 2810 K, the peaks of Rh_2O_3(II)-type phase became more intense. On the other hand, the peaks of corundum again grew when we reduced the temperature to 1930 K. In a similar manner, we performed another heating cycles (#4 to #8), in which both forward (Corundum $\rightarrow$ Rh_2O_3) and reversal (Rh_2O_3 $\rightarrow$ Corundum) transitions were successfully observed (Table 1).

The change in stable structures with changing the *P-T* conditions is illustrated in chronological order in Fig. 4. From the results of these forward and backward experiments, we tightly constrain the location of the phase transition boundary between corundum and the Rh_2O_3(II)-type structure. The transition occurs above 106 GPa at 1800 K. The boundary has a negative *P/T* (Clapeyron) slope of -6.5 ± 1.5 MPa/K.

Boundary between Rh_2O_3(II) and $CaIrO_3$-type phases

120 We have conducted four separate runs (runs #2-5) up to a pressure of 193 GPa and a
121 temperature of 3540 K for Rh_2O_3(II)-$CaIrO_3$ boundary (Table 2). In run #2, we first synthesized
122 the Rh_2O_3(II)-type phase by heating corundum to 1900 K at 127 GPa. Only the Rh_2O_3(II)-type
123 structure was observed up to 157 GPa and 2570 K. The peaks from $CaIrO_3$-type phase appeared
124 when the sample was compressed and then again heated to 2590 K at 186 GPa for 32 min. In the
125 next experiment (run #3), the XRD pattern was collected only at 158 GPa and 3170 K, showing
126 the $CaIrO_3$-type structure. In run #4, the $CaIrO_3$-type phase was first obtained directly from
127 corundum at 164 GPa and 2990 K. We then further compressed this sample and reheated to
128 relatively low temperature (1850 K). The peaks from Rh_2O_3(II) appeared coexisting with the
129 $CaIrO_3$-type phase in 43 min. With such Rh_2O_3(II) + $CaIrO_3$ mixed sample, the stability of
130 Rh_2O_3(II) or $CaIrO_3$ was determined with changing the *P-T* conditions, based on the
131 growth/reduction of the XRD peaks. We used the peak areas of 211 and 310 lines and 022 and
132 131 lines for Rh_2O_3(II) or $CaIrO_3$-type phases, respectively (Table 2). Figs. 3c and 5a illustrate
133 the XRD pattern when the $CaIrO_3$ peaks extensively grew at 193 GPa and 3420 K. The
134 relatively intense $CaIrO_3$ peaks were also present at 149 GPa and 3510 K (Fig. 5b). In the
135 following heating at 143 GPa and 3540 K, we observed the growth of Rh_2O_3(II) peaks at the
136 expense of $CaIrO_3$ peaks (Fig. 5c). In the fifth run, a mixture of Rh_2O_3(II) and $CaIrO_3$-type

phases was obtained in the first heating at 159 GPa and 2840 K. On further heating to 2950 K, the peaks from $CaIrO_3$-type structure grew in 13 min.

These results are summarized in Fig. 6, in which the change in stable crystal structure is illustrated along with the experimental *P-T* path in each run. The location of the Rh_2O_3(II)-$CaIrO_3$ phase transition boundary is precisely determined from these data. The results show that the transition occurs at 170 GPa and 2300 K with a high negative Clapeyron slope of -20 ± 5 MPa/K.

DISCUSSION

These data are compared with earlier theoretical and experimental reports in Fig. 7. Our results on corundum-Rh_2O_3(II) boundary are generally consistent with the experimental studies by Funamori and Jeanloz (1997) and Lin et al. (2004), although the transition boundary was not well constrained in these earlier experiments. Both pressure and the negative Clapeyron slope of the boundary are in excellent agreement with the GGA calculations by Tsuchiya et al. (2005), although their LDA results show much lower transition pressure.

Present experiments demonstrate that the phase transition between Rh_2O_3(II)- and $CaIrO_3$-type structures occurs at 170 GPa and 2300 K (Fig. 7). Such transition pressure and the

high negative Clapeyron slope are again in general agreement with the GGA calculations reported by Tsuchiya et al. (2005). On the other hand, the transition pressure determined here is much higher than that reported by previous experiments performed by Ono et al. (2006), who reported the transition pressure of ~130 GPa at 1500 K. Such discrepancy is in part because of the difference in pressure scale used to estimate the experimental pressure. Ono and others used Au pressure scale (pressure-volume-temperature equation of state) proposed by Jamieson et al. (1982), while we calculated the pressure based on the Pt pressure scale by Holmes et al. (1989). Akahama et al. (2002) have shown that Jamieson's Au scale gives the pressure lower by ~20 GPa at ~150 GPa and 300 K than Holmes's Pt scale used in the present experiments. Internally-consistent Au and Pt pressure scales were proposed by Fei et al. (2007) and Dorogokupets and Dewaele (2007). These scales help to diminish the discrepancy between the results by Ono et al. (2006) and this study, but the difference in Rh_2O_3(II)-$CaIrO_3$ transition pressure is still found to be ~30 GPa.

More importantly, we found that phase transitions in Al_2O_3 are rather sluggish. The $CaIrO_3$-type phase appeared in 32 min by heating the single phase Rh_2O_3(II) sample to 2590 K (#7 in Fig. 6). Similarly, we observed the appearance of Rh_2O_3(II)-type phase after heating the single-phase $CaIrO_3$ sample for 43 min (#11 in Fig. 6). Ono et al. (2006) synthesized

171 $CaIrO_3$-type Al_2O_3 from the corundum starting material at ~170 GPa and 2000-2500 K, which
172 is consistent with the present study. Ono and co-workers reheated this $CaIrO_3$-type Al_2O_3 with
173 decreasing pressure and observed the phase transition to Rh_2O_3(II)-type structure below 130
174 GPa and 2000 K. They suggested the transition pressure to be ~130 GPa only from such $CaIrO_3$
175 $\rightarrow$ Rh_2O_3(II) experiments. However, the low transition pressure reported by Ono et al. (2006)
176 may be due to the effect of kinetic hindering of the reaction and should be confirmed by reversal
177 experiments. The kinetic problem may have been significant in the experiments by Ono and
178 others because they mixed the Al_2O_3 sample with gold powder that served as a laser absorber.
179 Since metal powder easily becomes aggregate upon laser-heating, such sample preparation
180 often causes heterogeneous temperature distributions (Sinmyo and Hirose 2010). In contrast to
181 their experiments, we determined the *P*-*T* location of the boundary mainly using the Rh_2O_3(II)
182 + $CaIrO_3$ coexisting sample in order to avoid such a kinetic problem. Moreover, present result
183 was constrained by both forward and backward reactions. We also used metal-coated samples
184 in this study, which provided homogeneous temperature distributions upon laser heating. All of
185 these efforts should have helped in obtaining the equilibrium phase transition boundary.

186 Present study demonstrates that phase transition between Rh_2O_3(II) and $CaIrO_3$-type
187 phases in Al_2O_3 does not take place in the mantle pressure range. This transition has been

188 suggested to occur in subducted primordial crust with anorthosite composition or highly
189 Al-rich sediments (Komabayashi et al. 2009; Kawai et al. 2009). Moreover, Kawai and others
190 argued that such subducted anorthositic crust is dense in the lowermost mantle, and the negative
191 Clapeyron slope of the Rh_2O_3(II)–$CaIrO_3$ transition disturbs recycling and thus causes
192 accumulation of anorthositic crust in the core-mantle boundary region. However, without
193 Rh_2O_3(II)–$CaIrO_3$ transition in Al_2O_3 phase, the density of anorthositic crust is comparable to
194 that of pyrolitic lower mantle. It is therefore likely that the anorthositic primordial crust was
195 easily involved in the mantle convection and is not an important constituent in the present D"
196 layer.

197

198 **ACKNOWLEDGMENTS**

199 We thank N. Sata for technical support. The synchrotron XRD experiments were
200 performed at BL10XU, SPring-8 (proposals no. 2009B0087 and 2010A0087). Comments from
201 the Associate Editor and two anonymous referees were helpful to improve the manuscript.

202

203 **REFERENCES CITED**

204 Akahama, Y., Kawamura, H., and Singh, A.K. (2002) Crosscheck of Pt and Au Pressure Scales

and EOS of Bi to Megabar Pressures. The Review of High Pressure Science and Technology, 12, 63-68 (in Japanese with English abstract).

Akber-Knutson, S., Stein-Neumann, G., and Asimow, P.D. (2005) Effect of Al on the sharpness of the $MgSiO_3$ perovskite to post-perovskite phase transition. Geophysical Research Letters, 32, L14303, DOI: 10.1029/2005GL023192.

Caracas, R. and Cohen, R.E. (2005) Prediction of a new phase transition in Al_2O_3 at high pressures. Geophysical Research Letters, 32, L06303, DOI: 10.1029/2004GL022204.

Cohen, R.E. (1987) Calculation of elasticity and high pressure instabilities in corundum and stishovite with the potential induced breathing model. Geophysical Research Letters, 14, 37-40, DOI: 10.1029/GL014i001p00037.

Dorogokupets, P.I., and Dewaele, A. (2007) Equations of state of MgO, Au, Pt, NaCl-B1, and NaCl-B2: internally consistent high-temperature pressure scales. High Pressure Research, 27, 431-446.

Duan, W., Wentzcovitch, R.M., and Thomson, K.T. (1998) First-principles study of high-pressure alumina polymorphs. Physical Review B, 57, 10363-10369.

Fei, Y., Ricolleau, A., Frank, M., Mibe, K., Shen, G., and Prakapenka, V. (2007) Toward an internally consist pressure scale. Proceedings of National Academy of Sciences USA, 104,

9182-9186.

Funamori, N. and Jeanloz, R. (1997) High-pressure transformation of Al_2O_3. Science, 278, 1109-1111.

Hammersley, A.P., Svensson, S.O., Hanfland, M., Fitch, A.N., and Hausermann, D. (1996) Two-dimensional detector software: From real detector to idealised image or two-theta scan. High Pressure Research, 14, 235-248.

Hirose, K. (2006) Postperovskite phase transition and its geophysical implications. Reviews of Geophysics, 44, RG3001, DOI: 10.1029/2005RG000186.

Holmes, N.C., Moriarty, J.A., Gathers, G.R., and Nellis, W.J. (1989) The equation of state of platinum to 660 GPa (6.6 Mbar). Journal of Applied Physics, 66, 2962-2967.

Jamieson, J.C., Fritz, J.N., and Manghnani, M.H. (1982) Pressure measurement at high temperature in X-ray diffraction studies: gold as a primary standard. In S. Akimoto and M.H. Manghnani, Eds., High Pressure Research in Geophysics, p. 27-48. Reidel, Boston.

Jephcoat, A.P., Hemley, R.J., and Mao, H.K. (1988) X-ray diffraction of ruby (Al_2O_3:Cr^{3+}) to 175 GPa. Physica B, 150, 115-121.

Kawai, K., Tsuchiya, T., Tsuchiya, J., and Maruyama, S. (2009) Lost primordial continents. Gondwana Research, 16, 581-586.

239 Komabayashi, T., Maruyama, S., and Rino, S. (2009) A speculation on the structure of the D″
240 layer: The growth of anti-crust at the core–mantle boundary through the subduction history
241 of the Earth. Gondwana Research, 15, 342-353.
242 Lin, J.F., Degtyareva, O., Prewitt, C.T., Dera, P., Sata, N., Gregoryanz, E., Mao, H.K., and
243 Hemley, R.J. (2004) Crystal structure of a high-pressure/high-temperature phase of alumina
244 by *in situ* X-ray diffraction. Nature Materials, 3, 389-393.
245 Marton, F.C. and Cohen, R.E. (1994) Prediction of a high-pressure phase transition in Al_2O_3.
246 American Mineralogist, 79, 789-792.
247 Oganov, A.R. and Ono, S. (2005) The high-pressure phase of alumina and implications for
248 Earth's D″ layer. Proceedings of the National Academy of Sciences of the United States of
249 America, 102, 10828-10831.
250 Ohishi, Y., Hirao, N., Sata, N., Hirose, K., and Takata, M. (2008) Highly intense
251 monochromatic X-ray diffraction facility for high-pressure research at SPring-8. High
252 Pressure Research, 28, 163-173.
253 Ono, S., Oganov, A. R., Koyama, T., and Shimizu, H. (2006) Stability and compressibility of
254 the high-pressure phases of Al_2O_3 up to 200 GPa: Implications for the electrical
255 conductivity of the base of the lower mantle. Earth and Planetary Science Letters, 246,

326-335.

Sinmyo, R. and Hirose, K. (2010) The Soret diffusion in laser-heated diamond-anvil cell. Physics of the Earth and Planetary Interiors, 180, 172-178.

Tateno, S., Hirose, K., Sata, N., and Ohishi, Y. (2005) Phase relations in $Mg_3Al_2Si_3O_{12}$ to 180 GPa: Effect of Al on post-perovskite phase transition. Geophysical Research Letters, 32, L15306, DOI: 10.1029/2005GL023309.

Thomson, K.T., Wentzcovitch, R.M., and Bukowinski, M.S.T. (1996) Polymorphs of alumina predicted by first principles: Putting pressure on the ruby pressure scale. Science, 274, 1880-1882.

Tsuchiya, J. and Tsuchiya, T. (2008) Postperovskite phase equilibria in the $MgSiO_3$–Al_2O_3 system. Proceedings of the National Academy of Sciences of the United States of America, 105, 19160-19164.

Tsuchiya, J., Tsuchiya, T., and Wentzcovitch, R.M. (2005) Transition from the Rh_2O_3(II)-to-$CaIrO_3$ structure and the high-pressure-temperature phase diagram of alumina. Physical Review B, 72, 020103(R).

Figure captions

FIGURE 1. Examples of temperature profile across the laser-heated spot at 96-192 GPa. X-ray diffraction was collected from 15-μm area around the hot spot.

FIGURE 2. XRD patterns of Al_2O_3 + Pt obtained at (a) 87 GPa and 300 K before heating, (b) 105 GPa and 2180 K, and (c) 102 GPa and 1870 K. C, corundum; R, Rh_2O_3(II)-type phase; Pt, platinum; S, SiO_2 phase (pressure medium).

FIGURE 3. Caked-two-dimensional diffraction image was taken at (a) 102 GPa and 1870 K, (b) 105 GPa and 2180 K, and (c) 192 GPa and 3420 K, corresponding to XRD patterns shown in Figs. 2c, 2b, and 5a, respectively. Vertical bars indicate peak positions. C, corundum; R, Rh_2O_3(II)-type phase; PPv, $CaIrO_3$-type (post-perovskite-type) phase; Pt, platinum.

FIGURE 4. Phase boundary between corundum and Rh_2O_3(II)-type phase in Al_2O_3. Sequential change in the experimental *P*-*T* conditions is illustrated by numbers (see the first column in Table 1). Solid tie-lines show the actual *P*-*T* path, while broken lines indicate the reheating after compression/decompression at room temperature (press load was changed in between). Solid squares, corundum; open circles, Rh_2O_3(II)-type structure.

FIGURE 5. XRD patterns of Al_2O_3 + Pt, obtained at (a) 192 GPa and 3420 K, (b) 148 GPa and 3510 K, and (c) 142 GPa and 3540 K. R, Rh_2O_3(II)-type phase; PPv, $CaIrO_3$-type (post-perovskite-type) phase; A, α-PbO_2-type SiO_2; Pt, platinum.

FIGURE 6. Phase boundary between Rh_2O_3(II)-type and $CaIrO_3$-type (post-perovskite-type) structures in Al_2O_3. Sequential change in the *P*-*T* conditions is illustrated by numbers (see the first column in Table 2) and tie-lines (broken lines indicate that the load pressure was changed in between). Open, solid, and half-filled symbols indicate Rh_2O_3(II)-type, $CaIrO_3$-type, and Rh_2O_3(II) + $CaIrO_3$ coexisting, respectively. Circles, run #2; diamond, run #3; squares, run #4; triangles.

FIGURE 7. Comparison of present experimental results (solid squares, corundum; open circles, Rh_2O_3(II)-type phase; sold diamonds, $CaIrO_3$-type phase) with previous experiments and calculations. Dash-dotted line denotes the Rh_2O_3(II)-$CaIrO_3$ boundary determined experimentally by Ono et al. (2006). Blue and red zones represent the calculated corundum-Rh_2O_3(II) and Rh_2O_3(II)-$CaIrO_3$ boundaries, respectively (the range indicates the difference between the LDA and GGA results) from Tsuchiya et al. (2005).

TABLE 1. Experimental conditions and results. The growth of XRD peaks indicates the stability of corundum (Co) or Rh_2O_3(II)-type (Rh) phase

	Cycle#	Heating (min)	a_{Pt} (Å)	*P* (GPa)	*T* (K)	X-ray	Change in Co/Rh ratio*
1	1	8	3.6900(9)	98.9(23)	2390	Co growth	Co only
2	2	38	3.6464(6)	120.6(24)	2060	Rh appearance	→0.49
3	3	8	3.6726(10)	105.2(21)	2180	Rh growth	2.94→1.93
4	3	15	3.6740(11)	102.2(19)	1870	Co growth	1.93→2.74
5	3	2	3.6737(9)	107.2(23)	2560	Rh growth	2.74→2.00
6	3	10	3.6741(8)	108.7(24)	2810	Rh growth	2.00→1.32
7	3	4	3.6768(9)	101.1(18)	1930	Co growth	1.32→3.06
8	4	7	3.6651(9)	107.2(18)	1820	Rh growth	3.06→2.55
9	4	9	3.6652(9)	108.4(19)	2000	Rh growth	1.40→0.79
10	5	4	3.6639(9)	106.4(16)	1600	Co growth	0.56→2.21
11	5	5	3.6627(10)	107.6(18)	1670	Rh growth	2.21→0.95
12	5	11	3.6622(11)	109.1(19)	1850	Rh growth	0.95→0.77
13	5	14	3.6623(12)	114.3(25)	2560	Rh growth	0.77→0.62
14	6	3	3.6898(9)	99.9(25)	2900	Rh growth	1.92→0.86
15	6	40	3.6967(6)	96.9(24)	3000	Co growth	0.86→2.08
16	7	8	3.6833(7)	103.1(24)	2840	Rh growth	2.08→1.12
17	7	12	3.6826(4)	105.0(23)	3050	Rh growth	1.12→0.43
18	8	45	3.6899(4)	102.4(24)	3190	Rh growth	0.75→0.63
19	8	23	3.6892(5)	97.9(20)	2480	Co growth	0.63→1.22
20	8	16	3.6888(4)	96.6(18)	2270	Co growth	1.22→1.45

Note: Numbers in parentheses are uncertainty in the last digit(s).

* The ratio was calculated based on the peak areas of 104 line and 211 and 021 lines for corundum and Rh_2O_3(II)-type, respectively. The sample position possibly changed between different heating cycles.

303

304

TABLE 2. Experimental conditions and results. The growth of XRD peaks indicates the stability of Rh_2O_3(II) (Rh) or $CaIrO_3$-type (PPv) phase

	Run	Cycle#	Heating (min)	a_{Pt} (Å)	*P* (GPa)	*T* (K)	X-ray	Change in Rh/PPv ratio*
1	2	1	16	3.6350(12)	127.1(26)	1900	Rh appearance	Rh only
2	2	1	9	3.6371(11)	128.9(27)	2380	Rh growth	Rh only
3	2	2	21	3.6157(12)	142.3(30)	2140	Rh growth	Rh only
4	2	2	11	3.6144(12)	145.3(31)	2460	Rh growth	Rh only
5	2	3	3	3.5992(14)	153.9(32)	2040	Rh growth	Rh only
6	2	3	3	3.6002(12)	157.1(34)	2570	Rh growth	Rh only
7	2	4	32	3.5653(10)	186.0(27)	2590	PPv appearance	→3.59
8	2	4	6	3.5658(12)	187.5(30)	2870	PPv growth	3.59→2.03
9	3	1	13	3.6028(10)	158.4(29)	3170	PPv appearance	
10	4	1	12	3.5943(14)	164.0(28)	2990	PPv appearance	
11	4	2	43	3.5678(15)	178.7(25)	1850	Rh appearance + PPv growth	
12	4	2	31	3.5641(20)	192.8(39)	3420	PPv growth	2.49→0.15
13	4	3	8	3.5820(5)	169.7(19)	2290	Rh growth	0.15→0.24
14	4	4	6	3.6224(14)	142.6(29)	2850	Rh growth	0.29→0.70
15	4	4	7	3.6211(10)	145.3(30)	3110	Rh growth	0.70→1.11
16	4	4	7	3.6195(8)	148.9(32)	3510	PPv growth	1.11→0.68
17	4	5	23	3.6296(5)	142.5(27)	3540	Rh growth	0.68→0.90
18	4	6	10	3.6049(10)	156.3(28)	2980	Rh growth	0.89→1.58
19	4	7	6	3.5891(8)	163.4(21)	2240	Rh growth	2.07→2.58
20	5	1	5	3.5995(6)	159.4(21)	2840	Rh + PPv appearance	
21	5	1	13	3.5971(5)	161.9(25)	2950	PPv growth	5.65→3.59

Note: Numbers in parentheses are uncertainty in the last digit(s).

* The ratio was calculated based on the peak areas of 211 and 310 lines and 022 and 131 lines for Rh_2O_3(II)-type and $CaIrO_3$-type, respectively. The sample position possibly changed between different heating cycles.

305

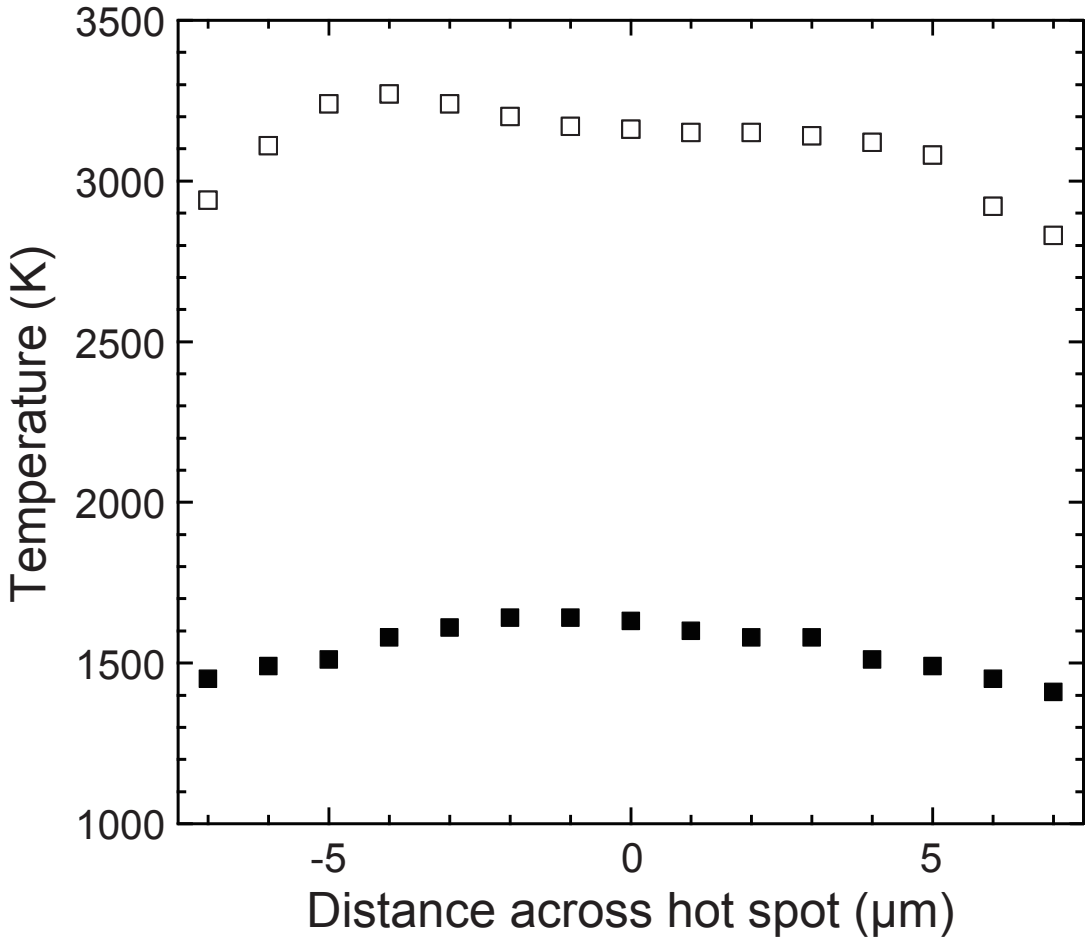
3500
3000
2500
2000
1500
1000
Temperature (K)
-5
0
5
Distance across hot spot (μm)

figure 1

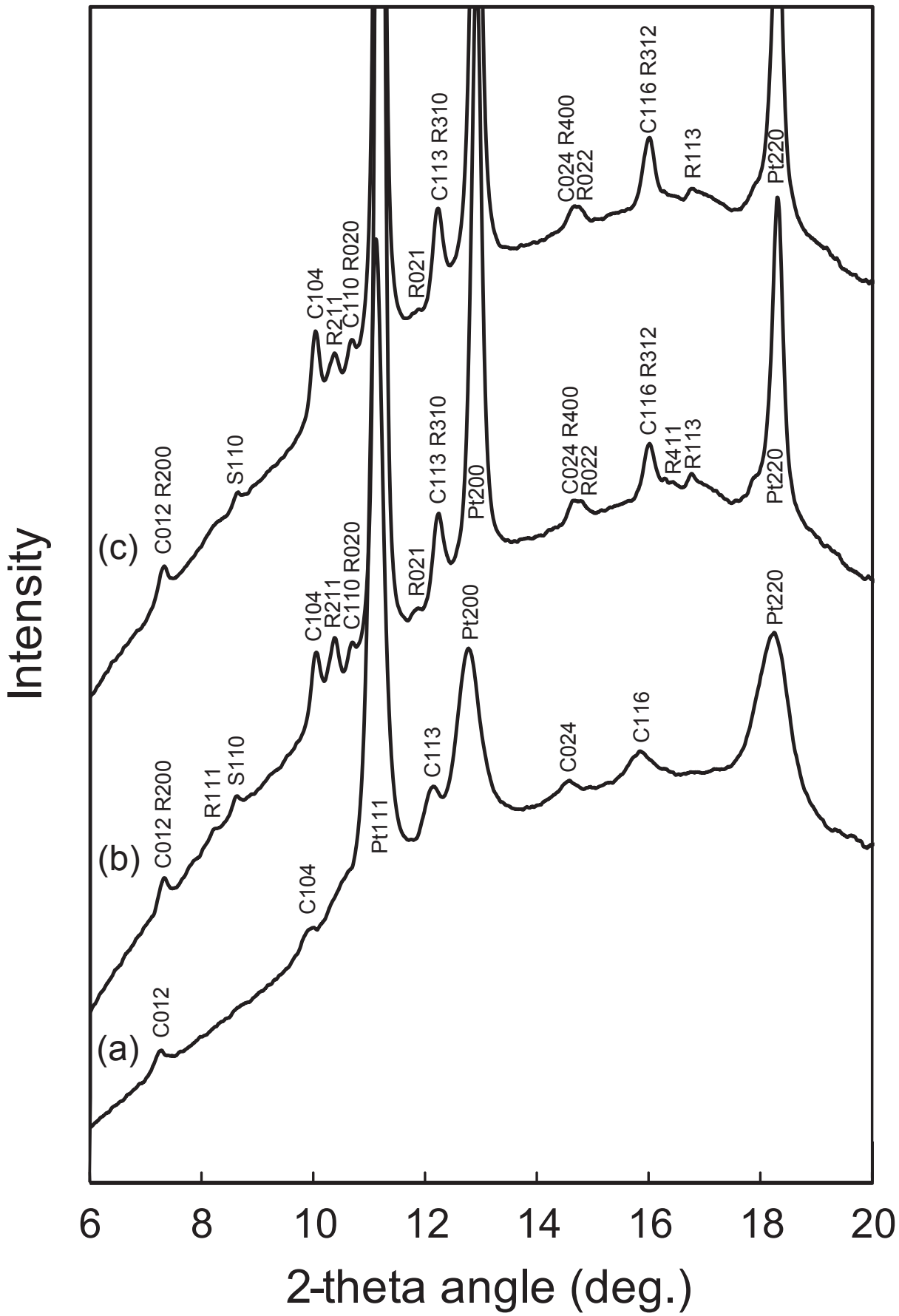
Intensity
(a)
(b)
(c)
C012
C104
Pt111
C012 R200
R111
S110
C104
R211
C110 R020
R021
C113
Pt200
C024
C116
Pt220
C012 R200
S110
C104
R211
C110 R020
R021
C113 R310
Pt200
C024 R400
R022
C116 R312
R411
R113
Pt220
C012 R200
S110
C104
R211
C110 R020
R021
C113 R310
Pt200
C024 R400
R022
C116 R312
R113
Pt220
6
8
10
12
14
16
18
20
2-theta angle (deg.)

figure 2

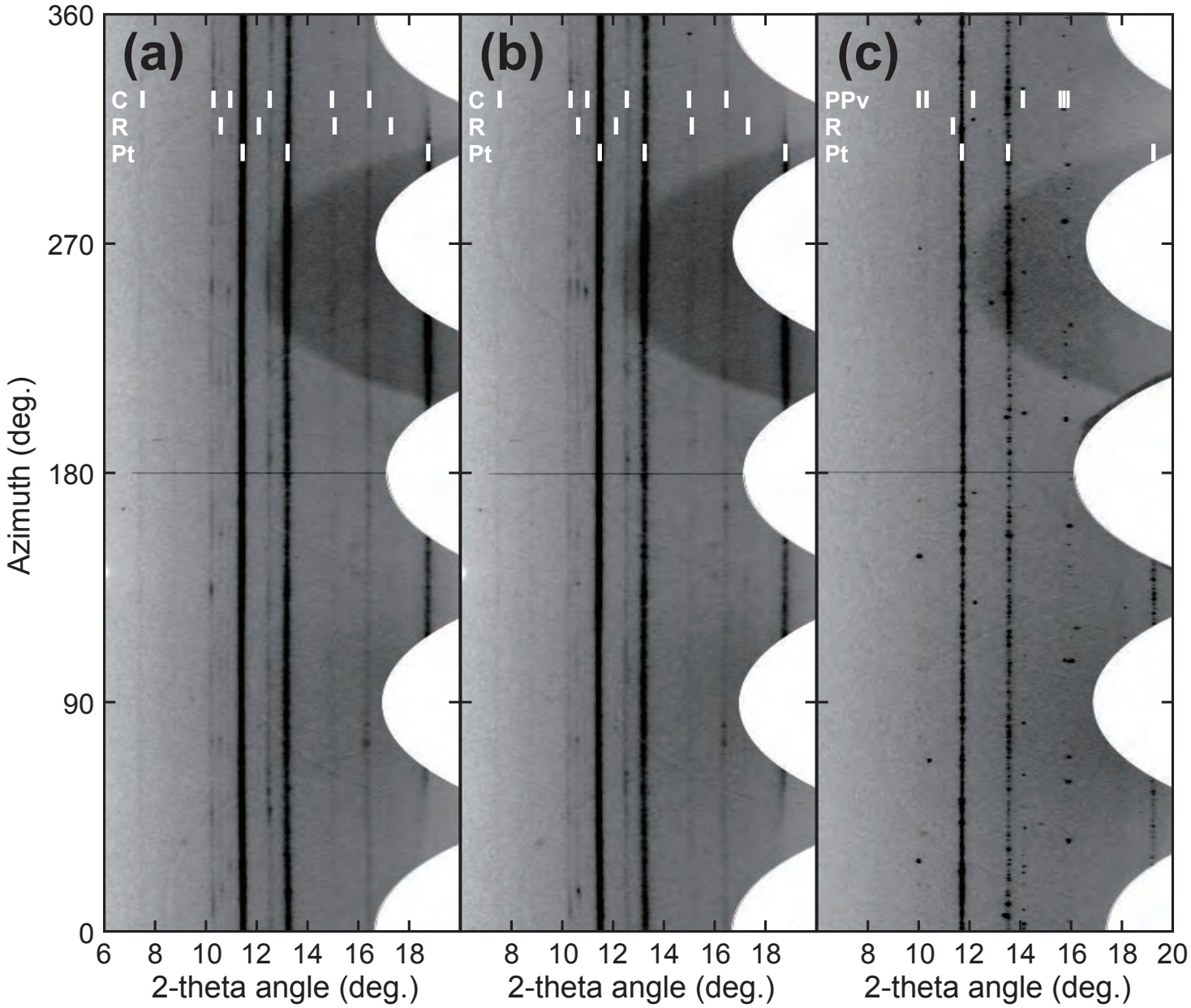
(a)
C
R
Pt
(b)
C
R
Pt
(c)
PPv
R
Pt
Azimuth (deg.)
360
270
180
90
0
6 8 10 12 14 16 18
2-theta angle (deg.)
8 10 12 14 16 18
2-theta angle (deg.)
8 10 12 14 16 18 20
2-theta angle (deg.)

figure 3

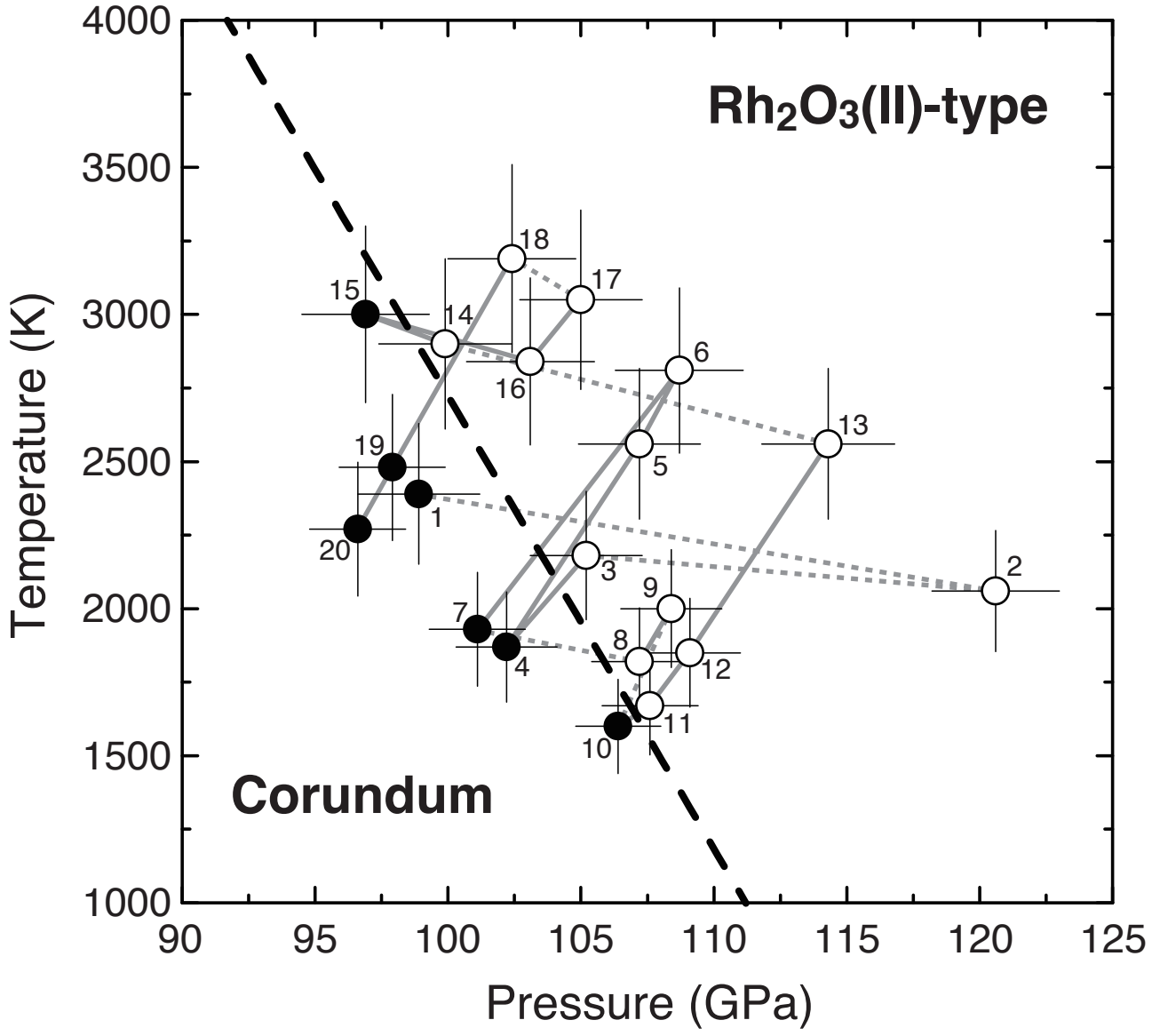
Rh2O3(II)-type
Corundum
Temperature (K)
Pressure (GPa)
4000
3500
3000
2500
2000
1500
1000
90
95
100
105
110
115
120
125
1
2
3
4
5
6
7
8
9
10
11
12
13
14
15
16
17
18
19
20

figure 4

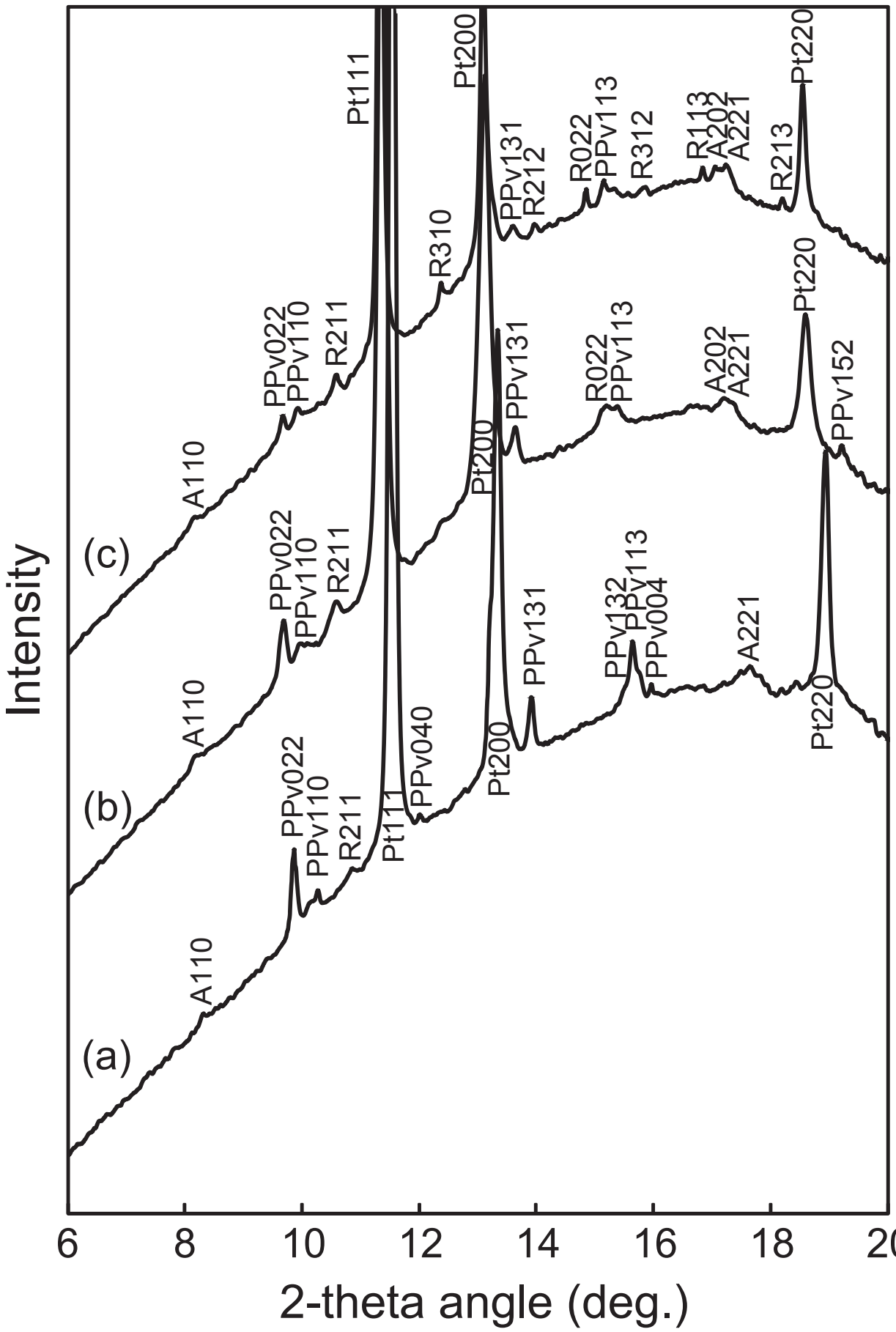
Intensity
2-theta angle (deg.)
6
8
10
12
14
16
18
20
(a)
(b)
(c)
A110
PPv022
PPv110
R211
Pt111
PPv040
Pt200
PPv131
R212
R310
R022
PPv113
R312
R113
A202
A221
R213
Pt220
PPv132
PPv004
PPv152

figure 5

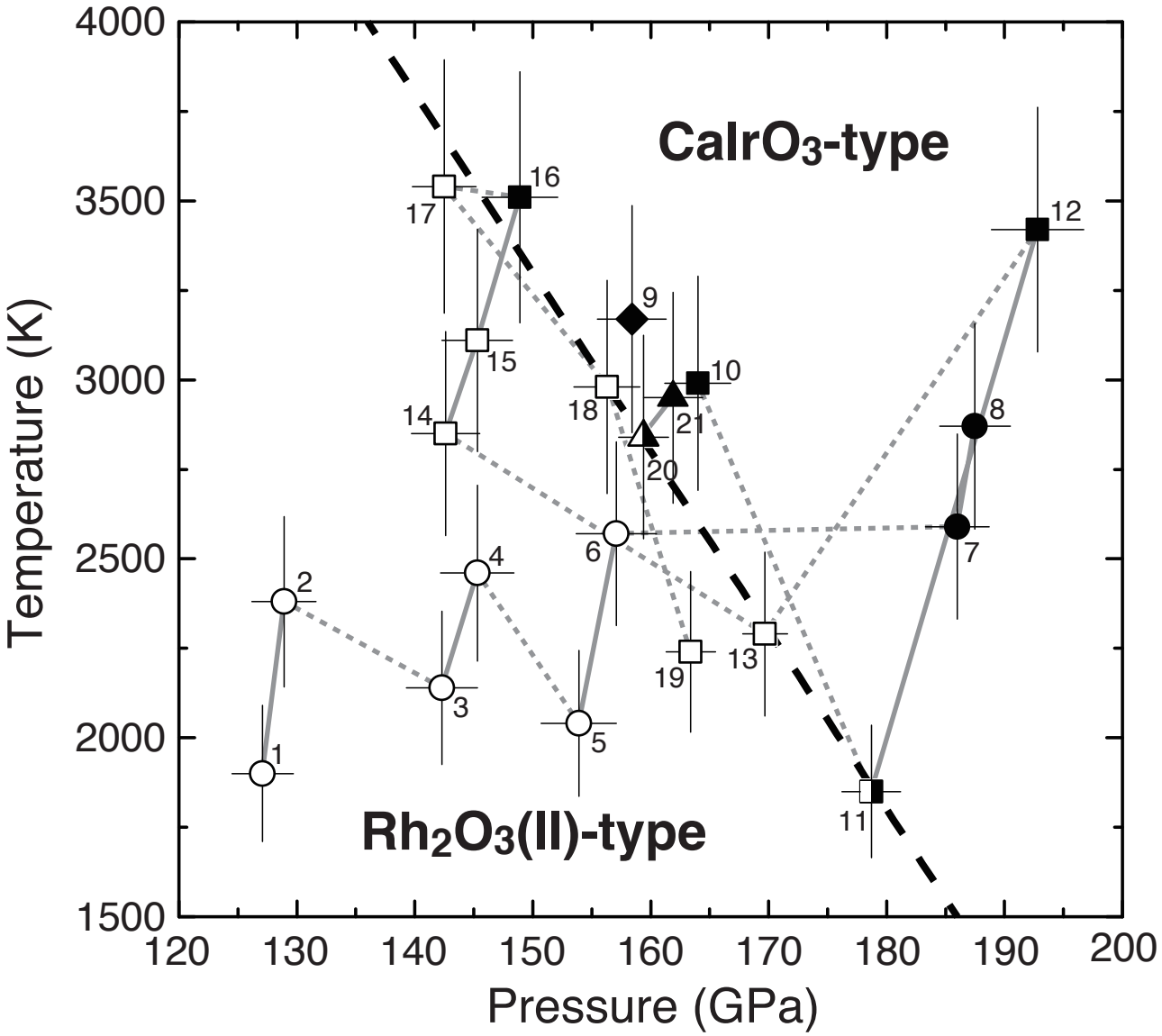
CaIrO3-type
Rh2O3(II)-type
Temperature (K)
Pressure (GPa)
4000
3500
3000
2500
2000
1500
120
130
140
150
160
170
180
190
200
1
2
3
4
5
6
7
8
9
10
11
12
13
14
15
16
17
18
19
20
21

figure 6

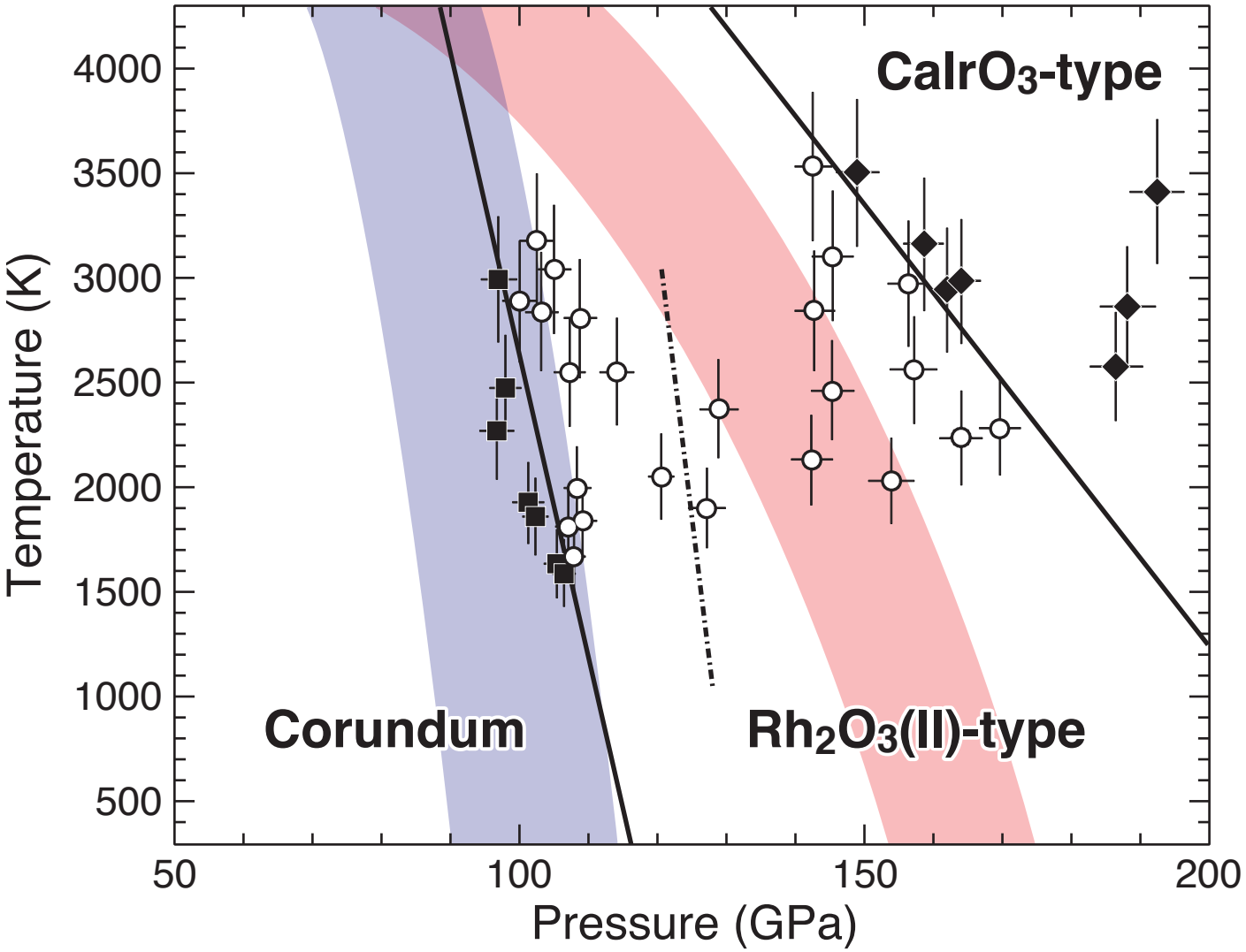
CaIrO3-type
Corundum
Rh2O3(II)-type
Temperature (K)
Pressure (GPa)
4000
3500
3000
2500
2000
1500
1000
500
50
100
150
200

figure 7